FERMILAB-CONF-73-114-E

UR-432

COO-3065-44

PROTON-PROTON COLLISIONS AT 102 GeV/c*

P. Slattery

Department of Physics and Astronomy

University of Rochester

Rochester, New York 14627

*Research supported by U. S. Atomic Energy Commission.

PROTON-PROTON COLLISIONS AT 102 GeV/c*

P. Slattery
University of Rochester, Rochester, N.Y. 14627

ABSTRACT

Preliminary results from an analysis of 102 GeV/c proton-proton collisions using the NAL 30 inch bubble chamber are discussed. Single particle inclusive spectra for the reactions $pp \to p + \ldots$ and $pp \to \pi^{\pm} + \ldots$ are presented, and comparisons are made with corresponding data from other high energy experiments carried out both using NAL and lower energy accelerators.

INTRODUCTION

The opening talks at this conference are all based on studies of proton-proton collisions carried out using the NAL 30 inch bubble chamber. To date, exposures have been made at three different energies: 102 GeV/c[1], 205 GeV/c[2], and 303 GeV/c[3], and a fourth is scheduled for 405 GeV/c[4]. In order to minimize duplication in these talks, it has been informally decided among these speakers to present the available data by physics topic, rather than energy-by-energy. Consequently, in this talk I will not only be discussing results obtained at 102 GeV/c (Table I lists the physicists contributing to this experiment), but I will also be presenting some data obtained in the other two NAL 30 inch bubble chamber proton-proton exposures. It should always be clear to which experimental group each result presented should be attributed.

Table I List of Contributing Physicists

102 GeV/c pp Collisions	
University of Michigan	University of Rochester
J. Chapman	C. Bromberg
N. Green	D. Cohen
B. Roe	T. Ferbel
A. Seidl	P. Slattery
J. Vander Velde	

THE REACTION $pp \to p + \ldots$

The utility of the 30 inch bubble chamber for studying the reaction $pp \to p + \ldots$ may most conveniently be discussed by means of Fig. 1. In this figure are displayed contours of constant proton lab momentum plotted versus the cm variables $x = 2P_{\ell}^{*}/\sqrt{s}$ and P_t^2.

*Research supported by U. S. Atomic Energy Commission.

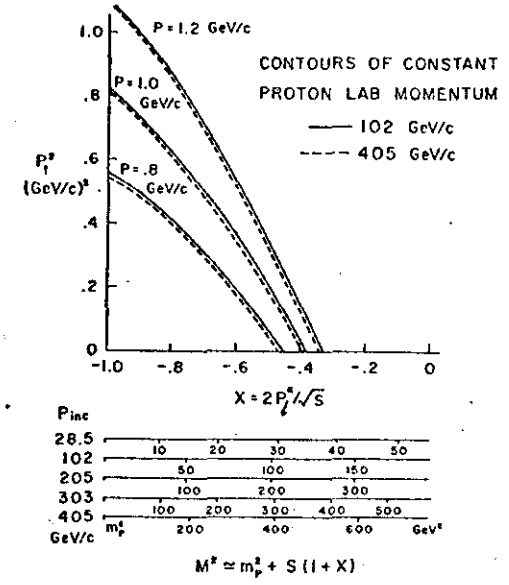

Fig. 1. Contours of constant proton lab momentum.

contours displayed in Fig. 1 are moreover only weakly energy dependent as illustrated by the extremely slight variation occurring between 102 and 405 GeV/c.

Except in the vicinity of $x = 0$, the squared mass (M^2) recoiling from the identified proton is related to x by $M^2 \simeq m_p^2 + s(1 + x)$, where $s \simeq 2m_p (P_{inc} + m_p)$, m_p is the proton mass, and P_{inc} is the magnitude of the beam momentum. Using this relationship, mass squared scales have also been drawn on Fig. 1 for various values of P_{inc} pertinent to this talk. As can readily be seen, in the NAL energy range, experimental biases

Since protons with lab momenta $P \lesssim 1.2$ GeV/c can routinely be identified in a bubble chamber via visual estimates of ionization, we have that the region below and to the left of the outer curve in Fig. 1 may be studied in an unbiased manner in even a small bubble chamber. Due to the rapid P_t^2 fall-off of physical data (this characteristic is illustrated for the 102 GeV/c data in Fig. 2; note that the slope of the experimental P_t^2 distribution (~ 7.5 (GeV/c)$^{-2}$) does not appear to be a strong function of the missing mass recoiling against the identified proton), we hence obtain the important result that the experimental biases introduced by the above momentum cutoff remain essentially negligible for $x \lesssim -.5$. At high incident momenta, the

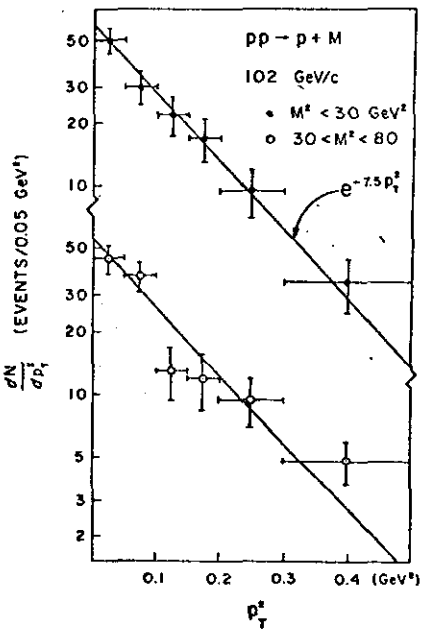

Fig. 2. P_T^2 distribution at 102 GeV/c.

only set in for very high M^2 values.

Figure 3 presents the observed M^2 spectra for the 3 presently available NAL pp experiments as well as for lower energy data with $P_{inc} = 28.5$ GeV/c [5] (in this and in all subsequent figures elastic scattering events have been removed). The distributions displayed are unbiased except at 28.5 GeV/c, where the cut-off at high M^2 values is an effect of the restriction to $P \lesssim 1.2$ GeV/c. The 3 high energy experiments are each characterized by low mass peaks standing out clearly against relatively smooth "background" distributions. While it is unclear at each energy just how much of these peaks to assign to any particular process, the data presented are consistent with the hypothesis that what is being observed is the production, with an approximately energy independent cross section of 6 ± 1 mb, of a low mass enhancement plus a steadily decreasing background contribution.

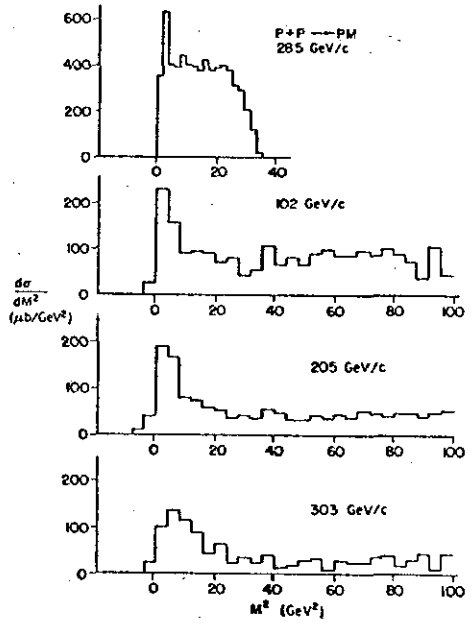

Fig. 3. Distribution of $\frac{d\sigma}{dM^2}$ at 28.5, 102, 205, and 303 GeV/c.

The observed widths of the peaks in the 3 NAL experiments are worthy of special note. At a given value of s, δM^2 is approximately independent of M^2, and varies linearly with s and consequently, at these energies, also linearly with P_{inc}. At 102 GeV/c, $\delta M^2 \simeq .7$ GeV^2 (this was in part estimated using elastic scattering events), and therefore at 205 and 303 GeV/c, $\delta M^2 \simeq 1.4$ and 2.1 GeV^2, respectively. Since the bin widths in Fig. 3 are 4 GeV^2, the observed peak widths are consequently experimentally significant. Two points should therefore be noted: (1) the peaking is a qualitatively different phenomenon from what is observed at lower energies since it spans a very much wider mass range; and, (2) the observed broadening of the experimental peaks with increasing beam momentum is genuine.

The variation of the M^2 spectra with charged prong multiplicity for each of these experiments is displayed in Fig. 4. While statistics are clearly a problem, the general trend appears to be for the 2 prong component to be decreasing between 102 and 303 GeV/c [6], while there is perhaps some indication of a 6 prong peak beginning to develop at 303 GeV/c. (The 4 prong component appears to pass through a <u>minimum</u> at 205 GeV/c; this may merely be an indication of the

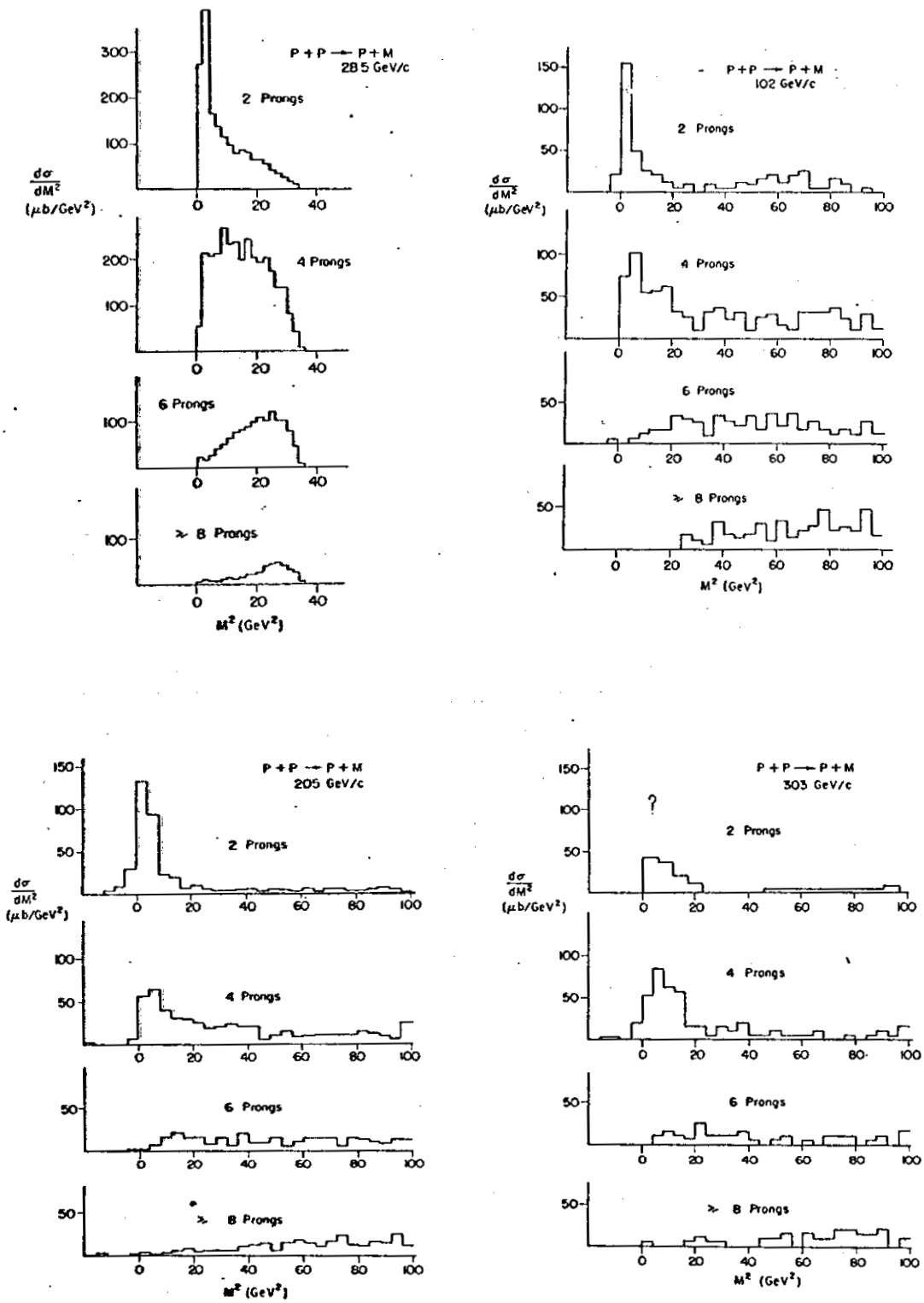

Fig. 4. Distribution of $\frac{d\sigma}{dM^2}$ versus charged prong multiplicity at 28.5, 102, 205, and 303 GeV/c. (See footnote 6.)

difficulties inherent in attempting to draw reliable conclusions from statistically limited data samples!)

The peripheral nature of the observed low mass enhancement is already apparent from Fig. 2. More detailed evidence is presented in Fig. 5 in which momentum transfer distributions for the 4 prong events from the 205 GeV/c experiment are presented. (This experiment has presently the highest statistics of the 3 NAL pp exposures, and the 4 prong data is uncontaminated by elastic scattering events.) While the very lowest M^2 sample has the steepest t distribution ($\frac{d\sigma}{dt} \propto e^{-9.25t}$), the slopes of the t distributions for the higher M^2 data do not display any strong M^2 dependence ($\frac{d\sigma}{dt} \propto e^{-4t}$). (The effects of $t_{min} \simeq (\frac{M^2 - m_p^2}{2P_{inc}})^2$ are not significant except for the very highest M^2 band displayed.)

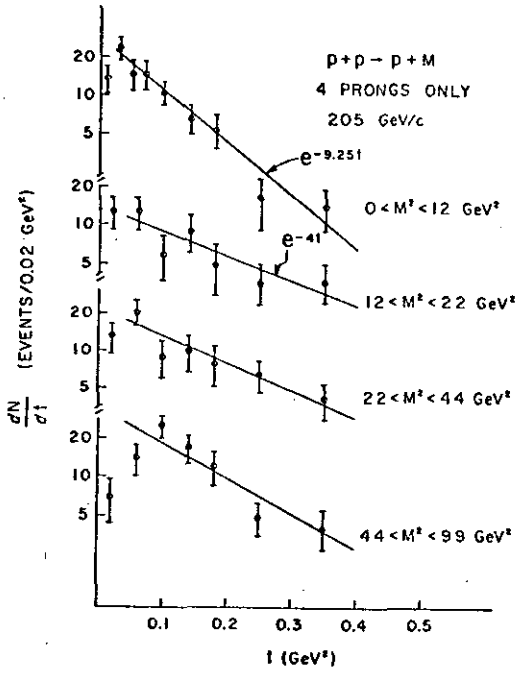

Fig. 5. t distribution for 4 prongs at 205 GeV/c.

This combination of characteristics: the threshold nature of the observed enhancements, the approximate energy independence of their production, and their highly peripheral nature, all justify the label "diffractive." We are consequently led naturally to conclude from these data that there exists strong evidence for a diffractive component in high energy proton-proton collisions.

It is of interest to inquire whether this observation is consistent with the previously noted onset of semi-inclusive scaling in this same energy range[7]. In Fig. 6 is displayed for reference the currently published evidence for the scaling behavior of the charged particle multiplicity distribution. The figure displays the quantity $\langle n \rangle \frac{\sigma_n}{\sigma_{inel}}$ versus $\frac{n}{\langle n \rangle}$ for data at 50, 69, 102, 205 and 303 GeV/c. A single smooth curve may be drawn through all of the data points with a very satisfactory χ^2 of 47 for 47 degrees of freedom. (The insert in the figure compares data at 19 GeV/c with a phenomenological curve describing the higher energy data; semi-inclusive scaling clearly only sets in at Serpukov energies and above.) Figure 7 presents in more detail some of the consequences of assuming exact semi-inclusive scaling for high energy charged particle multiplicity

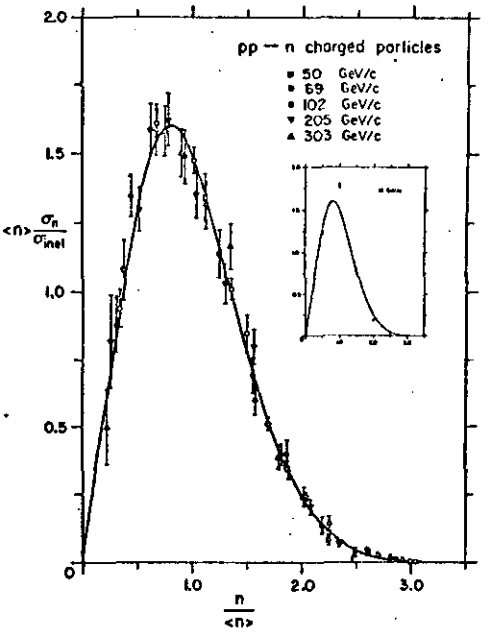

Fig. 6. Distribution of $\langle n\rangle \frac{\sigma_n}{\sigma_{inel}}$ versus $\frac{n}{\langle n\rangle}$ for charged particles produced at 50, 69, 102, 205, and 303 GeV/c. (See text.)

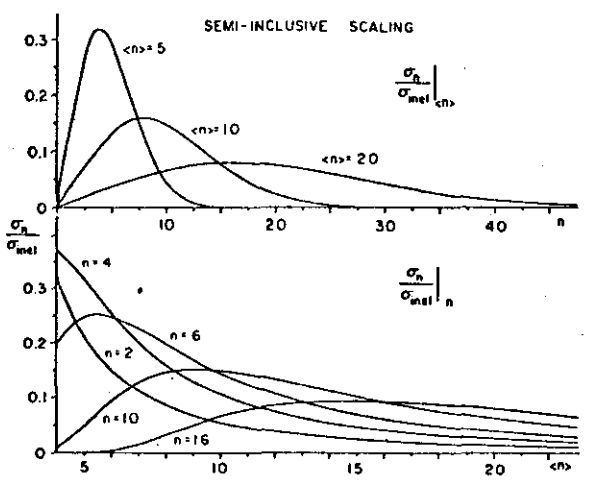

Fig. 7. Some consequences of assuming exact semi-inclusive scaling.

distributions. The top curves show the predicted multiplicity distributions for a few representative values of $\langle n\rangle$, while the lower set of curves show the variation with $\langle n\rangle$ of the partial cross sections for several charged prong multiplicities. The significant point to note is that $\frac{\sigma_n}{\sigma_{inel}}$ is single peaked at all energies; alternatively, this requires that $\frac{\sigma_n}{\sigma_{inel}} \to 0$ as $\langle n\rangle \to \infty$. The only way this prediction can be consistent with a "two component" picture of high energy pp collisions, in which the (approximately constant) inelastic part of the total cross section at very high energies is made up of fixed fractions of both diffractive and non-diffractive parts, is for both processes to yield charged prong multiplicity distributions which change similarly with energy (otherwise, double peaking would clearly have to set in at some value of $\langle n\rangle$). The, admittedly somewhat weak, experimental evidence that the average charged particle multiplicity for events in the diffractive peak may indeed be increasing with energy may be an indication that this is in fact the actual situation.

So far I have chosen to discuss the reaction $pp \to p + \ldots$ in terms of $\frac{d\sigma}{dM^2}$. Alternatively, one can choose to display these data as is done in Fig. 8

in which the invariant cross section $s\frac{d^2\sigma}{dM^2dt}$ is integrated over t and plotted versus $x \simeq 1 - M^2/s$. (The data points displayed in this figure have been calculated directly from Fig. 3; hence, the binning in x varies from experiment to experiment.) The significant features depicted in this figure are the fact that away from $x \simeq -1$, the high energy experiments exhibit approximate scaling behavior (to ~15%), and also that lower energy data approaches this "limit" from above. These observations are completely consistent with the higher statistics results of the Rutgers-Imperial College-Upsala College-Illinois collaborative experiment at fixed values of t (0.33 and 0.45 GeV^2).[8] It should be noted that comparing data at fixed x involves comparing very different values of M^2, and vice-versa; the points of view are clearly complementary, which one proves ultimately to be the more informative remains to be established.

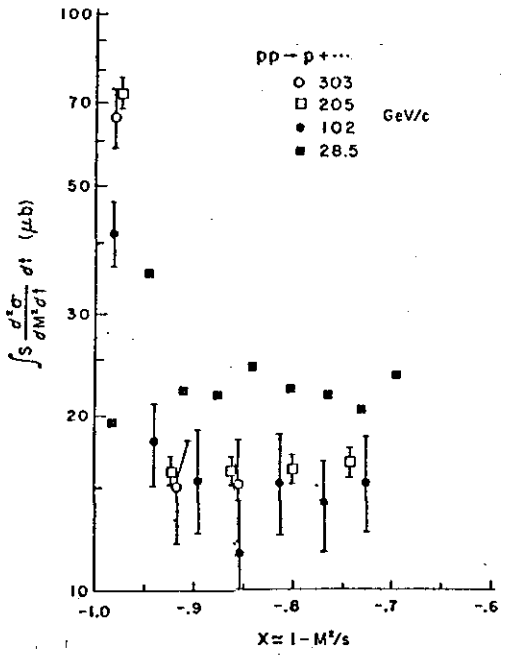

Fig. 8. Distribution of $\int \frac{d^2\sigma}{dM^2dt} dt$ versus x at 28.5, 102, 205, and 303 GeV/c.

THE REACTIONS $pp \to \pi^{\pm} + \ldots$

Figure 9 dramatically illustrates the value of a bubble chamber for disentangling a highly complex interaction. The event depicted has 18 charged prongs emanating from the production vertex, a neutron-induced 3 prong secondary, and a visible K^0 decay. All charged tracks can be clearly distinguished, and while its analysis was somewhat tedious, this event has been completely measured and geometrically reconstructed in space. In this section of my talk I will be discussing a sample of ~500 such events, spanning all topological classes, which have been completely measured and spatially reconstructed. (Corrections have been made for the very small number of events for which an unambiguous reconstruction could not be achieved.) Before presenting the experimental results on the reactions $pp \to \pi^{\pm} + \ldots$, however, I will begin by first discussing the impact on these measurements of the experimental resolution which can be achieved using just the bare 30 inch chamber at these very high energies.

I will ultimately be discussing the inclusive pion spectra in terms of the rapidity variable $y = \frac{1}{2}\log(\frac{E + P_L}{E - P_L})$. Figure 10 summarizes most of the kinematics which will be important in the present discussion. In this sketch, the momentum of a relativistic particle is represented by a rectangular parallelepiped with edges of lengths P_L, P_T and m. As shown in the sketch, the front face diagonal of such a figure has length $\sqrt{P_L^2 + P_T^2} = P$ (the momentum of the particle); the end face diagonal has length $\sqrt{P_T^2 + m^2} = \mu$ (the "transverse mass" of the particle); and the body diagonal of the figure has length $\sqrt{P^2 + m^2} = E$ (the energy of the particle). By trigonometric manipulation it can be shown that $y = \frac{1}{2}\log(\frac{E + P_L}{E - P_L})$ is also equal to $-\log(\tan \phi/2)$, where ϕ is the angle between the body diagonal (E) and the long edge (P_L) of the figure ($\tan\phi = \mu/P_L$).[9] For very thin figures (i.e. for $m \ll P_T$), clearly $\phi \simeq \theta$, where θ is the angle between the front face diagonal (P) and the long edge (P_L) of the figure ($\tan\theta = P_T/P_L$). This yields the familiar approximation of the true rapidity by the "cosmic ray variable", $\eta = -\log(\tan\theta/2)$. For small values of P_T, however, (corresponding to parallelepipeds with widths comparable to their thicknesses), where the cross sections are the largest, the replacement of y by η always leads to an overestimate of y (i.e. the angle ϕ is always greater than the angle θ).

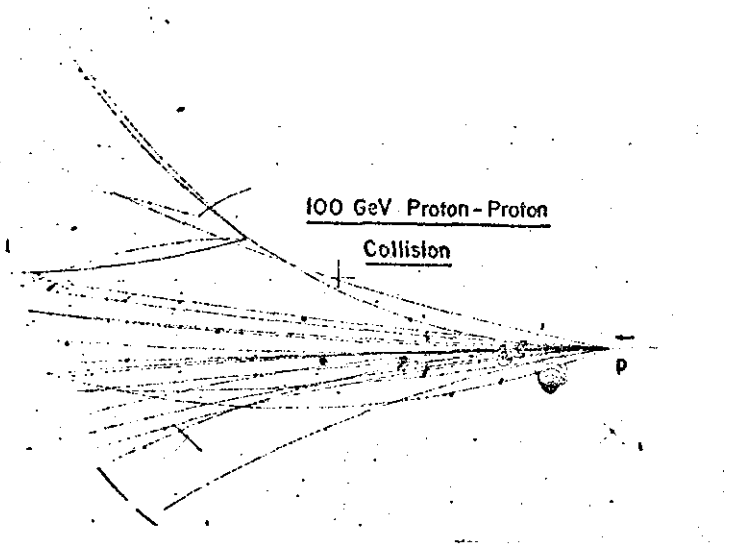

Fig. 9. High multiplicity event photographed in NAL 30 inch bubble chamber.

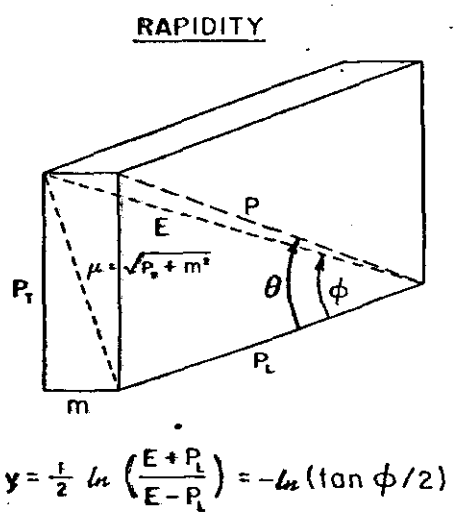

Fig. 10. Diagram illustrating geometrical definition of rapidity.

This can be a serious problem as can be seen from Fig. 11 in which are plotted Monte Carlo generated curves for pions distributed according to the function $e^{-y^2/a - P_t/b}$, where $a = \log(s/4m_p^2)$ and $b = 160$ MeV/c. The solid curves are the generated rapidity distributions, while the dashed curves are the corresponding η distributions. Clearly, the effect of replacing y by η is to significantly flatten the resulting distribution, and even to introduce a central dip at very high momenta. Since one of the interesting questions concerning the rapidity distribution is whether it is Gaussian or flat-topped[10], it clearly is significant which variable is being measured.

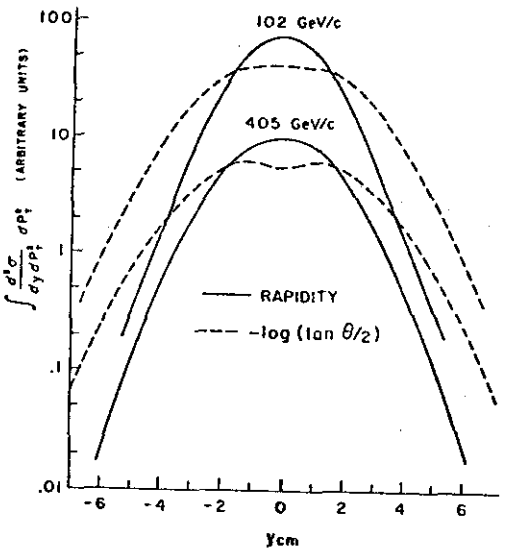

Fig. 11. Comparison between true rapidity and $-\log(\tan\theta/2)$.

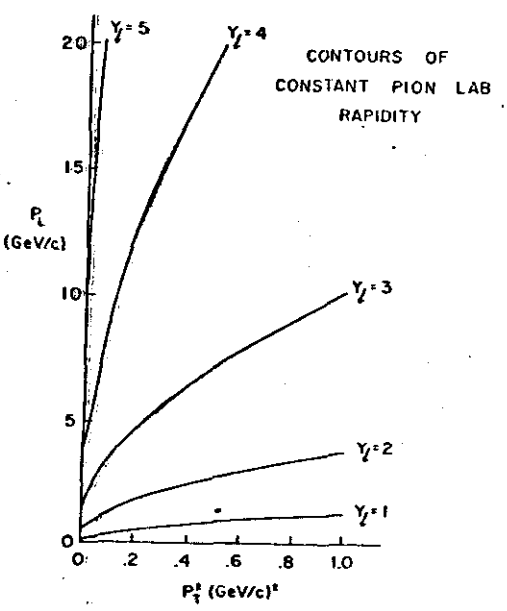

Fig. 12. Contours of constant pion lab rapidity.

The quantity η only depends on the angle of the track in question; to calculate y from η, however, requires a measurement of the track's momentum. Figure 12 displays contours of fixed lab rapidity versus the lab quantities P_L and P_T^2. Since $y_{lab} = y_{cm} + \frac{1}{2}\log(\frac{1+\beta}{1-\beta})$, where β defines the transformation from the lab to the cm frame, the given contours also represent fixed cm rapidities. Due to the overall symmetry of pp collisions, it suffices for this reaction to measure rapidities only up to $y_{cm} = 0$, which occurs for $y_{lab} = 2.69$, 3.04, 3.24, and 3.38 for $P_{inc} = 102$, 205, 303, and 405 GeV/c, respectively. As can be seen from Fig. 12, to go

much beyond these values of lab rapidity increasingly involves measuring many high momentum tracks for which accurate momentum determinations are not possible in a chamber as small as the 30 inch. This would appear to severely limit the usefulness of the device as far as non-symmetric reactions such as πp are concerned. Fortunately, the kinematic character of the rapidity variable counteracts this potential difficulty as can be seen from Fig. 13 in which contours of constant η_{lab} are plotted versus y_{lab} and P_{lab}. We note that except for low values of P_{lab}, which are measured very well in the 30 inch chamber, y_{lab} for fixed η_{lab} values is very insensitive to P_{lab} so even a crude momentum determination suffices to calculate y_{lab} from η_{lab} with

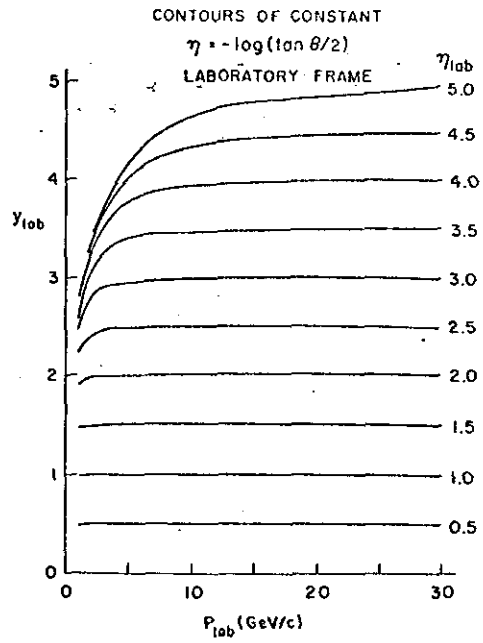

Fig. 13. Contours of constant $-\log(\tan\theta/2)$ in lab frame.

very high accuracy. (As a representative numerical example, for $\eta_{lab} = 3.5$ and $P_{lab} = 5$ GeV/c, even a 5% momentum determination suffices to determine y to better than .01.)

Figure 14 presents an illustration of the type of momentum resolution which is attainable for high momentum tracks in the 30 inch chamber. Depicted in this figure is the distribution of measured $k \simeq 1/p$ values for a sample of 102 GeV/c beam tracks. (The minimum length cutoff of 30 cm corresponds approximately to the limit imposed on secondary tracks by the fiducial volume employed in this experiment.) For purposes

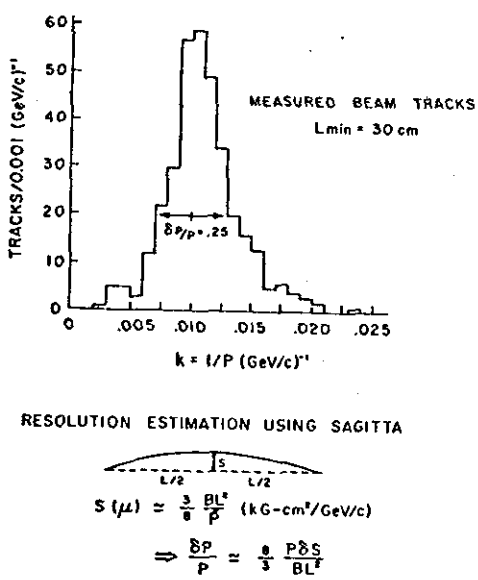

Fig. 14. Distribution of curvatures for measured beam tracks at 102 GeV/c.

of comparison, a first order estimate of $\delta p/p$ in terms of the sagitta is also outlined in Fig. 14; (for $\delta s = 50\mu$, $B = 27$ kG, and $L = 45$cm, we have $\delta p/p = 0.25$, which is approximately the width of the experimental k distribution.) Since for high momentum tracks $\delta p/p \propto p$, the resolution for typical secondary tracks is much better than this, and is clearly entirely adequate for an accurate determination of y_{lab}.

We may summarize this discussion of resolution as follows: The slopes of the curves shown in Fig. 13 are given by the formula $\left.\frac{\partial y}{\partial P}\right|_{\eta} = \frac{P_L/P}{E}\left(\frac{m}{\mu}\right)^2$. At high momenta this varies as $1/p^3$; consequently, the net dependence of δy on p for high momentum tracks decreases as $1/p$ (if angle errors are ignored). We therefore conclude that the resolution achievable using the bare 30 inch chamber is perfectly adequate for pion rapidity measurements; when one also takes into consideration the excellent pattern recognition capabilities of this chamber and its good resolution for low momentum tracks, it emerges that this device is in fact almost ideally suited for pion rapidity measurements!

Figure 15 presents the (folded) rapidity distributions for both positive and negative pions produced in 102 GeV/c pp collisions. (Before folding, each of these distributions was symmetric to within statistics.) The distributions shown have been corrected for $p^{\pm}$ and $K^{\pm}$ backgrounds; these corrections were carried out as follows. Low momentum protons were identified by ionization (as discussed in the first part of this talk). These tracks were removed from the sample (i.e. they are not included in Fig. 15); all other tracks were assumed to be pions. Using the sample of identified proton tracks plus the required symmetry of the overall distribution, an approximate, normalized, proton rapidity distribution was determined. Protons were generated according to this distribution, mis-interpreted as pions, and subtracted from the π^+ distribution shown in Fig. 15. This was the largest such correction applied ($\lesssim 10\%$). The smaller $\bar{p}$ and $K^{\pm}$ corrections were similarly determined except that Gaussian rapidity distributions were assumed for these particles;

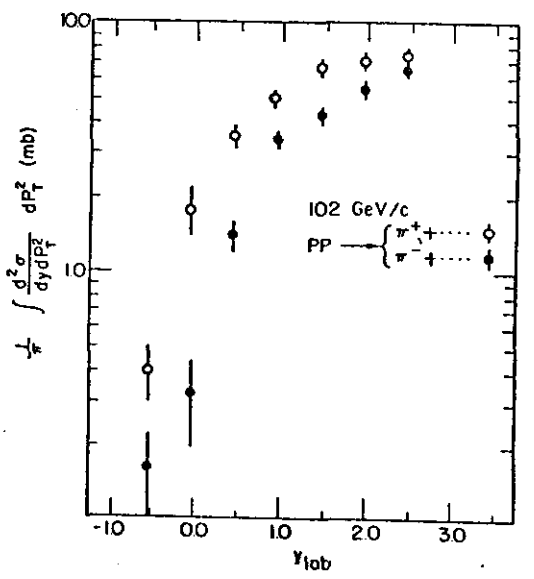

Fig. 15. Laboratory rapidity distributions for positive and negative pions at 102 GeV/c.

the normalizations for these distributions were estimated on the basis of the observed cross sections for K^0, Λ^0 and $\bar{\Lambda}^0$ production at 102 GeV/c. The error bars shown on the points in Fig. 15 include our estimates for the uncertainties in all of these corrections. The surplus of positive pions over negative pions in this figure is basically a reflection of the amount of neutron production in pp collisions.

Figure 16 compares the single particle inclusive rapidity spectra for the reaction $pp \to \pi^- + \ldots$ at 28.5, 102, and 205 GeV/c.[11] (No corresponding data at other energies was available for the reaction $pp \to \pi^+ + \ldots$.) The data are plotted in the lab frames at each of these energies and within statistics are seen to scale in the target fragmentation region. The data at 205 GeV/c do appear to exhibit some evidence for a possible plateau near $y_{cm} = 0$, but the error bars shown do not permit a Gaussian shape to be excluded at present.

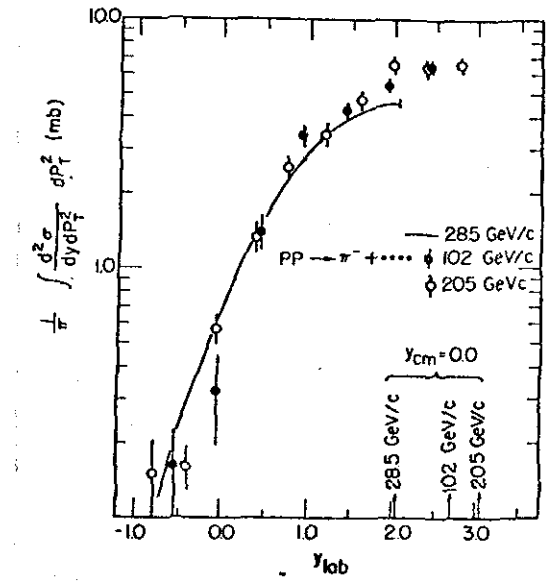

Fig. 16. Laboratory rapidity distributions for negative pions at 28.5, 102, and 205 GeV/c.

In keeping with my prior agreement with the next speaker, Jim Whitmore, I will leave the remainder of the discussion of the single particle inclusive pion spectra to him. It has been my primary intent here to simply present the new data along with enough of the experimental details to provide a background for his discussion.

I wish to thank J. Hanlon, J. Whitmore, and F. T. Dao, along with their collaborators, for making available to me unpublished pp data at 28.5, 205, and 303 GeV/c, respectively.

REFERENCES

1. Michigan-Rochester collaboration; see Table I for list of contributing physicists.
2. ANL-NAL collaboration; results presented at this conference by J. Whitmore.
3. NAL-UCLA collaboration; results presented at this conference by F. T. Dao and R. Poster.
4. Michigan-Rochester collaboration; this is the companion

experiment to the 102 GeV/c pp exposure.

5. BNL-Vanderbilt collatoration; private communication from J. Hanlon and R. Panvini.

6. Separating elastic and inelastic two prongs becomes increasingly difficult as the beam momentum is increased. The 303 GeV/c data given to me by F.T.Dao for this talk did not have the elastic events removed. However, in a paper delivered at the 1972 Winter APS meeting, and distributed as an NAL report (Dec. 26, 1972), E. Malamud presented an x distribution for 2 prong inelastic events from this experiment; I have used this x distribution in obtaining the M^2 distributions shown in Figs. 4 and 5. At present, the reliability of his elastic separation is in doubt (private communication from E. Malamud), and hence caution should be exercised in interpreting these data. It is my personal belief that the data are sufficiently reliable to support the basically qualitative conclusions reached in this talk.

7. Z. Koba, H.B. Nielsen, and P. Olesen, Nucl. Phys. B40, 317 (1972), first suggested, on theoretical grounds, that this type of scaling should asymptotically occur. The unexpected early onset of semi-inclusive scaling in the 50 to 303 GeV/c range of incident momentum was subsequently reported by P.Slattery, Phys.Rev. Letters 29, 1624 (1972) and Phys. Rev. D7, 2073 (1973).

8. F. Sannes et al., preprint (submitted to Phys. Rev. Letters), and also contributed to this conference.

9. This is an exact result and may be obtained as follows:

$$\frac{E + P_L}{E - P_L} = \frac{\sqrt{1 + \tan^2\phi} + 1}{\sqrt{1 + \tan^2\phi} - 1} = \frac{1 + \cos\phi}{1 - \cos\phi} = \frac{1}{\tan^2\phi/2} \quad .$$

10. See for example, P. Carruthers, Cornell University Preprint, CLNS-219 (1973).

11. The data at 205 GeV/c have also been corrected for K^- and $\bar{p}$ contamination; such corrections are less important at 28.5 GeV/c.